https://doi.org/10.5194/ms-2026-199
Preprint. Discussion started: 19 November 2026
© Author(s) 2026. CC BY 4.0 License.



mechanical sciences
DISCUSSIONS

Geometric Optimization of Sprag Overrunning Clutches for Improved Torque Capacity Based on Nonlinear Transient Analysis

Fahimeh Mashayekhi, Stefano Zucca, and Cristian Maria Firrone

Department of Mechanical and Aerospace Engineering, Politecnico di Torino, Corso Duca degli Abruzzi, 24, 10129 Turin, Italy

Correspondence: Fahimeh Mashayekhi (fahimeh.mashayekhi@polito.it)

Abstract. Sprag overrunning clutches provide one-way torque transmission in powertrains, but their performance during engagement is governed by nonlinear contact and frictional interactions. The strong coupling between geometric parameters, contact forces, and failure mechanisms makes it difficult to identify optimal designs through analytical approaches or conventional parametric studies. This study presents a failure-aware geometric-optimization framework that integrates nonlinear transient dynamic analysis to improve torque transmission performance while accounting for the competing design requirements. A displacement-based nonlinear dynamic model is employed to evaluate contact stress, slippage, and sprag rollover during transient loading. By combining this model with a genetic algorithm, the framework searches for a desired combination of five geometric parameters. A stress-weighted objective function favors higher failure-onset torque and lower contact stress, while geometric feasibility constraints are imposed. For fixed inner and outer race radii, the best design increases the slippage-onset torque by 42.8%, while reducing the corresponding maximum contact stress from 3.23 to 2.83 GPa, below the prescribed allowable limit. Under identical loading conditions, the optimized geometry also reduces contact stress and sprag rotation, but exhibits a lower frictional safety margin. Repeating the optimization with a reduced friction coefficient yields a different geometry with a higher frictional safety margin under nominal conditions, although at the expense of increased stress and rotation. These results demonstrate the potential of integrating transient dynamics with geometric optimization to identify improved clutch designs while revealing trade-offs between torque transmission and frictional robustness.

1 Introduction

Overrunning clutches transmit torque in one direction while allowing free relative rotation in the opposite direction. These operating modes are commonly referred to as the engaged and overrunning states, respectively. This functionality is valuable in power-transmission systems that require automatic and selective torque transfer. In a hybrid electric–turbine propulsion system, for example, an overrunning clutch can connect the electric motor to the propeller shaft when electric assistance is required and mechanically isolate the electric branch when the propeller is driven by the turbine (Pescetto et al., 2025; Bouchard et al., 2021; Nanda, 2011). For aerospace applications, sprag clutches must provide high torque capacity within limited installation space while maintaining reliable engagement during transient acceleration.

https://doi.org/10.5194/ms-2026-199
Preprint. Discussion started: 19 November 2026
© Author(s) 2026. CC BY 4.0 License.



mechanical sciences
DISCUSSIONS

Among different overrunning clutch types, sprag clutches are well suited to compact, high-speed, and high-torque applications (Kish, 1977). A sprag clutch consists of inner and outer races separated by an annular space containing spring-energized sprags. In the driving direction, the sprags rotate and wedge between the races, generating normal contact forces and transmitting torque through tangential contact forces. In the opposite direction, the sprags move toward a disengaged configuration and the clutch overruns.

The response of a sprag clutch is governed by geometric, contact, and frictional nonlinearities. Early analytical models described the locked condition through torque–windup relations, with contact forces obtained from Hertzian deformation and with rolling without slip imposed at the sprag–race contacts (Xu and Lowen, 1994). Such models are useful for estimating engaged-state stiffness, but they do not directly predict loss of sticking. Vernay later formulated state-dependent dynamic equations for a sprag-type freewheel clutch, distinguishing engaged and sliding phases. In the engaged phase, pure rolling kinematic constraints are imposed, while the friction condition is checked through the tangential-to-normal force ratio. If the friction limit is exceeded, the model switches to a separate sliding formulation (Vernay and Ferraris, 2006). Further studies improved contact-force and contact-stress prediction by including structural deformation, contact nonlinearity, edge effects, slice methods, rate-dependent friction laws, and axial loads (Ke et al., 2020; Huang et al., 2018; Nagler and Lohrengel, 2021). Recently, a displacement-based nonlinear transient model of sprag overrunning clutches was developed by the authors (Mashayekhi et al., 2026). The model accounts for the evolution of contact geometry and determines stick, slip, and lift-off without prescribing the contact state.

Previous studies have also investigated sprag-clutch geometric optimization, particularly to reduce contact stress under prescribed loading conditions (Huang et al., 2018; Ke et al., 2020). Although such approaches improve contact durability, they do not directly evaluate the torque that can be transmitted before the onset of engagement failure. Chen and Chen (2008) demonstrated that geometric modifications significantly affect contact forces, contact stresses, and slipping torque in roller-type overrunning clutches. In sprag clutches, the coupling between geometry, contact forces, and sprag rotation further complicates the identification of favorable designs.

Two important mechanisms that may limit torque transmission are slippage and rollover. Slippage occurs when the frictional force required to maintain sticking exceeds the available friction capacity, while rollover occurs when the sprag rotation exceeds its admissible geometric range (Lynwander et al., 1972). Classical design criteria based on the gripping or strut angle provide useful estimates of engagement conditions (for, 2018). However, the evolution of contact forces and sprag motion during transient acceleration also depends on contact compliance, spring preload, and powertrain dynamics. Consequently, these failure mechanisms must be evaluated in conjunction with the transient response.

In the present work, the recent framework for the dynamic analysis of a sprag overrunning clutch is used. It is, first, enhanced by replacing the linear normal contact law with a nonlinear Hertzian formulation and incorporating the radial dynamics of the inner and outer races and the sprag. These extensions enable the accurate evaluation of contact stresses and account for the influence of radial compliance on the transient contact response.

The dynamic model is integrated into a genetic algorithm to investigate the strongly nonlinear coupled relationship between the sprag geometry and torque-transmission performance. Five parameters defining the sprag cam profiles and centroid position

https://doi.org/10.5194/ms-2026-199
Preprint. Discussion started: 19 November 2026
© Author(s) 2026. CC BY 4.0 License.



mechanical sciences
DISCUSSIONS

are optimized while keeping the inner- and outer-race radii fixed. For each candidate geometry, the transient response is evaluated under a prescribed torque history until slippage or rollover is detected. A stress-weighted objective function favors geometries that sustain higher torque before failure while developing lower contact stress. The optimization therefore considers the competing effects of geometric modifications on torque transmission and contact loading.

The main contribution of this paper is the development of a geometric-optimization framework based on nonlinear transient dynamic analysis that accounts for engagement failure. The strong coupling between geometric parameters, contact forces, and failure mechanisms makes the identification of favorable designs challenging through analytical approaches or conventional parametric studies. Accounting for transient failure-onset in the optimization process, the proposed framework enables the identification of geometry combinations with improved torque-transmission capability, with the associated contact stress, rollover resistance, and frictional safety margin are evaluated. Section 2 presents the model extensions and optimization formulation, Section 3 describes the numerical implementation and results, and Section 4 summarizes the conclusions.

2 Methodology

The proposed framework combines a displacement-based transient model of the sprag clutch (Mashayekhi et al., 2026) with a constrained geometric optimization procedure. According to Vernay and Ferraris (2006); Xu and Lowen (1994); Ke et al. (2020), the model is enhanced to account for radial displacements and employ a nonlinear normal contact forces relation to improve the accuracy of the model, as discussed in Sec. 2.1. The integration of this model into the optimization process is discussed in Sec. 2.2.

2.1 The transient model of the sprag overrunning clutch

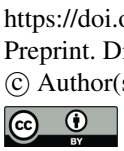
In a sprag overrunning clutch, each sprag interacts with the inner and outer races through two contact interfaces. The operating principle is governed by the eccentric rotation of the sprag: the instantaneous center of rotation of the sprag does not coincide with the centers of curvature of its cam surfaces. Consequently, sprag rotation modifies the normal relative displacement at the contact interfaces. Depending on the direction of relative motion, this variation either increases the normal indentation, promoting wedging and torque transmission, or reduces it, leading to slip or separation during overrunning.

2.1.1 Contact geometry of the sprag clutch

Two contact interfaces are defined for each sprag. Contact A denotes the interface between the sprag and the inner race, while contact B denotes the interface between the sprag and the outer race. For each interface, the contact geometry is described by the contact point, the local contact coordinate system, and the relative contact displacement expressed in terms of the generalized coordinates of the system.

The inner and outer races are modeled as radially flexible, whereas the sprags are assumed to be rigid. The system kinematics are described by the rotations and radial displacements of the inner and outer races, θ_I, θ_O, r_I, and r_O, together with the three sprag degrees of freedom, ϕ, α, and r_S, shown in Fig. 1. The coordinate ϕ represents the orbital rotation of the sprag reference

https://doi.org/10.5194/ms-2026-199
Preprint. Discussion started: 19 November 2026
© Author(s) 2026. CC BY 4.0 License.



mechanical sciences
DISCUSSIONS

point about the clutch center O, which is also the common center of the races. The coordinate α denotes the rotation of the sprag about its reference point, and r_S is its radial displacement.

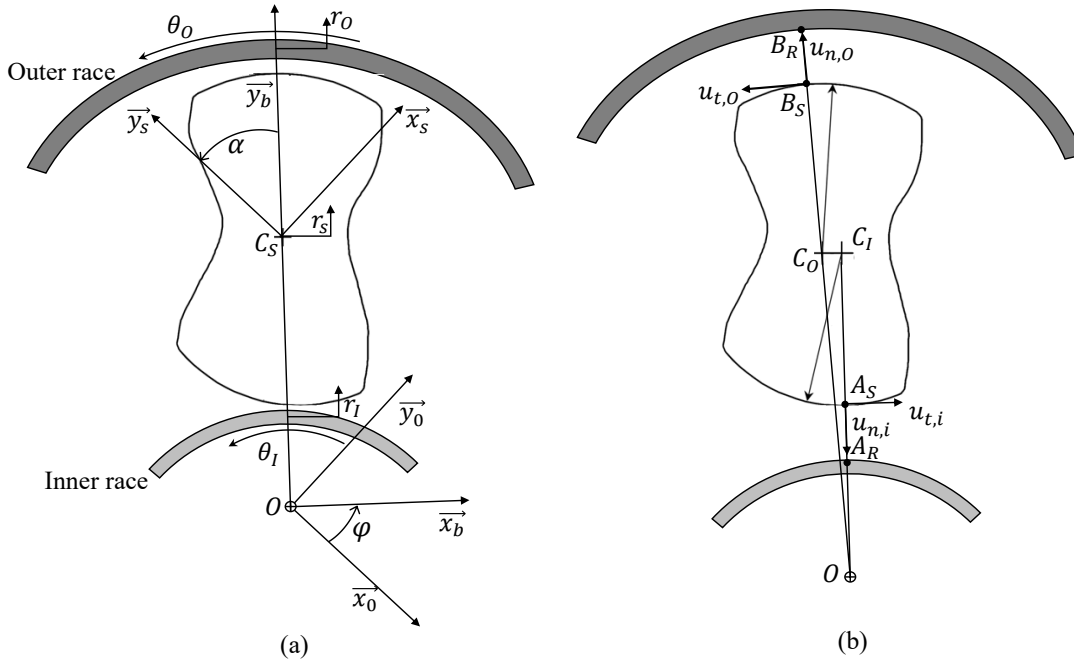


Figure 1. Clutch kinematics: (a) global coordinates and (b) local contact frames and displacement components.

Since the contact locations vary with sprag rotation, the contact points at interfaces A and B are updated at each time step from the instantaneous geometry. For the circular cam profiles considered in this work, the contact points are obtained from the intersections between the contact surfaces and the lines connecting the corresponding centers of curvature. The contact points on the sprag and race sides are denoted by A_S and A_R at the inner contact, and by B_S and B_R at the outer contact, where the subscripts S and R refer to the sprag and race, respectively. The local contact frames $(\mathbf{t}_A, \mathbf{n}_A)$ and $(\mathbf{t}_B, \mathbf{n}_B)$ are defined such that the normal directions are aligned with the corresponding local radii of curvature, while the tangential directions are perpendicular to them.

Based on this kinematic description, the incremental relative displacements at contacts A and B can be expressed in the corresponding local contact coordinate systems as

$$\begin{aligned}
\delta u_{t,B} &= \left(-\delta u_{t,B,\alpha} + \overline{OB_S}\,\delta\phi\right) - R_O\,\delta\theta_O + \delta r_{S,t,B}, \qquad \delta u_{n,B} = -\delta u_{n,B,\alpha} - \delta r_O + \delta r_{S,n,B}, \\
\delta u_{t,A} &= \left(\delta u_{t,A,\alpha} - \overline{OA_S}\,\delta\phi\right) + R_I\,\delta\theta_I - \delta r_{S,t,A}, \qquad \delta u_{n,A} = -\delta u_{n,A,\alpha} + \delta r_I - \delta r_{S,n,A}.
\end{aligned} \tag{1}$$

Here, $\overline{OA_S}$ and $\overline{OB_S}$ are the distances from the clutch center O to the sprag contact points A_S and B_S, respectively, while R_I and R_O are the inner- and outer-race radii. The terms $\delta u_{n,(\cdot),\alpha}$ and $\delta u_{t,(\cdot),\alpha}$ are the normal and tangential components of the

https://doi.org/10.5194/ms-2026-199
Preprint. Discussion started: 19 November 2026
© Author(s) 2026. CC BY 4.0 License.



mechanical sciences
DISCUSSIONS

contact-point displacement induced by the sprag rotation α. The incremental radial displacements of the inner and outer races are denoted by δr_I and δr_O, respectively. Finally, $\delta r_{S,t,(\cdot)}$ and $\delta r_{S,n,(\cdot)}$ denote the tangential and normal components of the incremental sprag displacement in the corresponding local contact frame.

The incremental displacements of the contact points caused by an infinitesimal rotation of the sprag are given by

$$\delta u_{B,\alpha} = \overline{CB_S}\,\delta\alpha, \qquad \delta u_{A,\alpha} = \overline{CA_S}\,\delta\alpha, \tag{2}$$

where $\overline{CA_S}$ and $\overline{CB_S}$ are the instantaneous distances between point C and the corresponding sprag contact points. These displacement vectors are perpendicular to the lines CA_S and CB_S, and they must be projected onto the local contact frames $(\mathbf{t}_A, \mathbf{n}_A)$ and $(\mathbf{t}_B, \mathbf{n}_B)$.

The sprag geometry adopted in this study is shown in Fig. 2. The parameters a_i and a_o define the positions of the inner and outer arc centers, C_I and C_O, relative to the sprag centroid C_S, while $R_{s,i}$ and $R_{s,o}$ are the corresponding cam radii. The auxiliary quantities used to evaluate the relative contact displacements are shown in Fig. 2(b).

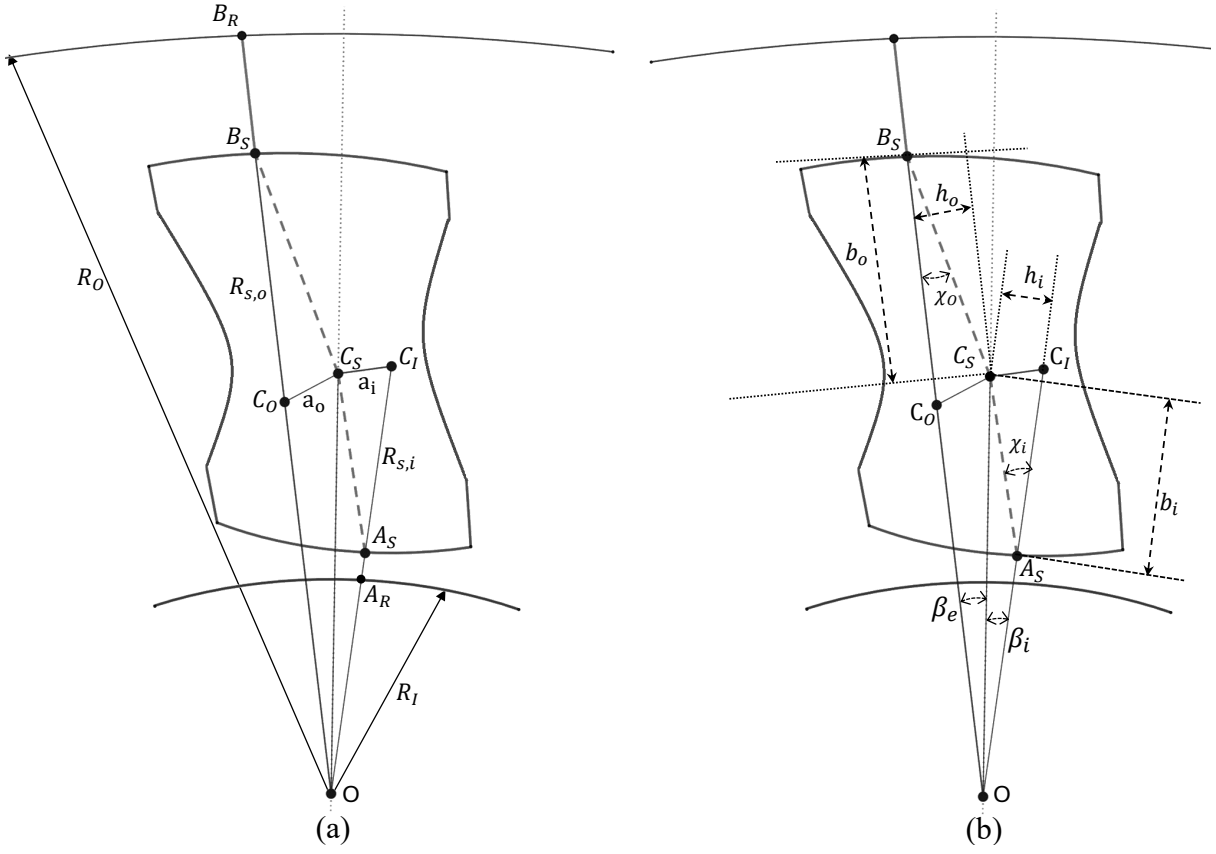


Figure 2. Sprag geometry: (a) design parameters a_i, a_o, $R_{s,i}$, $R_{s,o}$, R_I, and R_O and (b) auxiliary parameters b_i, b_o, h_i, h_o, χ_i, χ_o, β_i, and β_o.

https://doi.org/10.5194/ms-2026-199
Preprint. Discussion started: 19 November 2026
© Author(s) 2026. CC BY 4.0 License.



mechanical sciences
DISCUSSIONS

The auxiliary geometric quantities in Fig. 2(b) are computed from the clutch design parameters, as detailed in Appendix A. Once these quantities are known, the tangential and normal components of the incremental contact-point displacements induced by $\delta\alpha$ are obtained as

$$\delta u_{\mathrm{t},B,\alpha} = \overline{C_S B_S}\,\delta\alpha\cos(\chi_o), \qquad \delta u_{\mathrm{n},B,\alpha} = \overline{C_S B_S}\,\delta\alpha\sin(\chi_o),$$
$$\delta u_{\mathrm{t},A,\alpha} = \overline{C_S A_S}\,\delta\alpha\cos(\chi_i), \qquad \delta u_{\mathrm{n},A,\alpha} = \overline{C_S A_S}\,\delta\alpha\sin(\chi_i). \tag{3}$$

The angles χ_i and χ_o denote the angles between the lines connecting the sprag centroid C_S to the corresponding contact points and the local normal directions at the inner and outer contacts, respectively.

2.1.2 Displacement-based contact model

A compliant displacement-based contact model is adopted at each sprag–race interface, following (Menq and Yang, 1998; Petrov and Ewins, 2003). The normal contact force is computed from the local normal indentation, while the tangential contact force is updated from the incremental relative tangential displacement. During sticking, the tangential response is elastic. During sliding, the tangential force is limited by the Coulomb friction bound. This formulation allows the contact state to emerge from the instantaneous displacement and force conditions, without prescribing in advance whether the interface is stuck, sliding, or separated.

The contact force update is performed using a predictor–corrector procedure. First, the normal force is evaluated from the relative normal displacement. If the normal force is positive, a trial tangential force is computed under the sticking assumption. This trial force is then compared with the instantaneous Coulomb limit. If the trial force remains below the friction limit, the contact sticks; otherwise, the tangential force is corrected to the sliding value.

At each time step t, the normal force is evaluated using a Hertzian law,

$$N(t) = 2K_H[\max(u_n(t),0)]^{3/2}, \tag{4}$$

where $u_n(t)$ is the relative normal indentation and K_H is the Hertzian coefficient of one point contact. The factor of two accounts for the two axial point contacts used to represent each sprag–race interface, as discussed in Section 3. The operator $\max(\cdot,0)$ enforces the unilateral nature of the contact and prevents tensile normal forces.

If $N(t) = 0$, the contact is open and the tangential force is set to zero. Otherwise, the trial tangential force is evaluated as

$$T_p(t) = T(t-\Delta t) + K_t\,\delta u_t(t), \tag{5}$$

where $\delta u_t(t)$ is the incremental relative tangential displacement, K_t is the tangential contact stiffness, and $T(t-\Delta t)$ is the tangential force from the previous time step.

https://doi.org/10.5194/ms-2026-199
Preprint. Discussion started: 19 November 2026
© Author(s) 2026. CC BY 4.0 License.



mechanical sciences
DISCUSSIONS

The corrected tangential force is then obtained as

$$T(t) = \begin{cases} 0, & N(t) = 0, \quad \text{lift-off}, \\ T_p(t), & N(t) > 0 \text{ and } |T_p(t)| < \mu N(t), \quad \text{stick}, \\ \mu N(t)\,\mathrm{sign}(T_p(t)), & N(t) > 0 \text{ and } |T_p(t)| \geq \mu N(t), \quad \text{slip}. \end{cases} \tag{6}$$

Here, μ is the friction coefficient. The condition $|T_p(t)| \geq \mu N(t)$ provides a direct criterion for the onset of slippage at the considered contact interface.

For the sprag clutch, as shown in Fig. 3, each contact element is formulated in its local normal–tangential frame and is characterized by the Hertzian contact coefficient K_H and the tangential stiffness K_t.

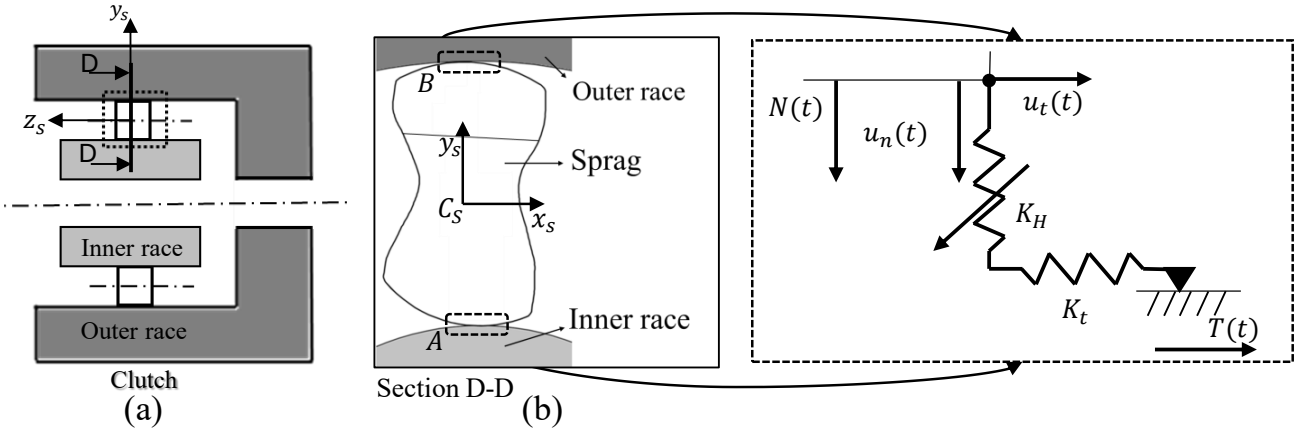


Figure 3. Displacement-based contact elements at the sprag–race interfaces.

2.1.3 Dynamic equations of motion

The sprag clutch is embedded in a lumped torsional powertrain model in order to evaluate the transient response during acceleration and torque transfer. The considered configuration consists of a motor connected to the inner race of the sprag clutch through an elastic shaft, and a propeller connected to the outer race through the output shaft. The response is analyzed in the time domain so that engagement, overrunning, and possible failure mechanisms can be captured within the same formulation. The adopted powertrain model is shown in Fig. 4(a).

The free-body diagram of the sprag is shown in Fig. 4(b). The sprag is subjected to the normal and tangential contact forces at the inner interface, denoted by (N_I, T_I), and at the outer interface, denoted by (N_O, T_O). In addition, the sprag is acted upon by the support-spring force F_r, which maintains the initial contact between the sprag and the races. The support spring force is applied at a fixed material point of the sprag P. As the sprag rotates as a rigid body about point C_S, the orientation of this

https://doi.org/10.5194/ms-2026-199
Preprint. Discussion started: 19 November 2026
© Author(s) 2026. CC BY 4.0 License.

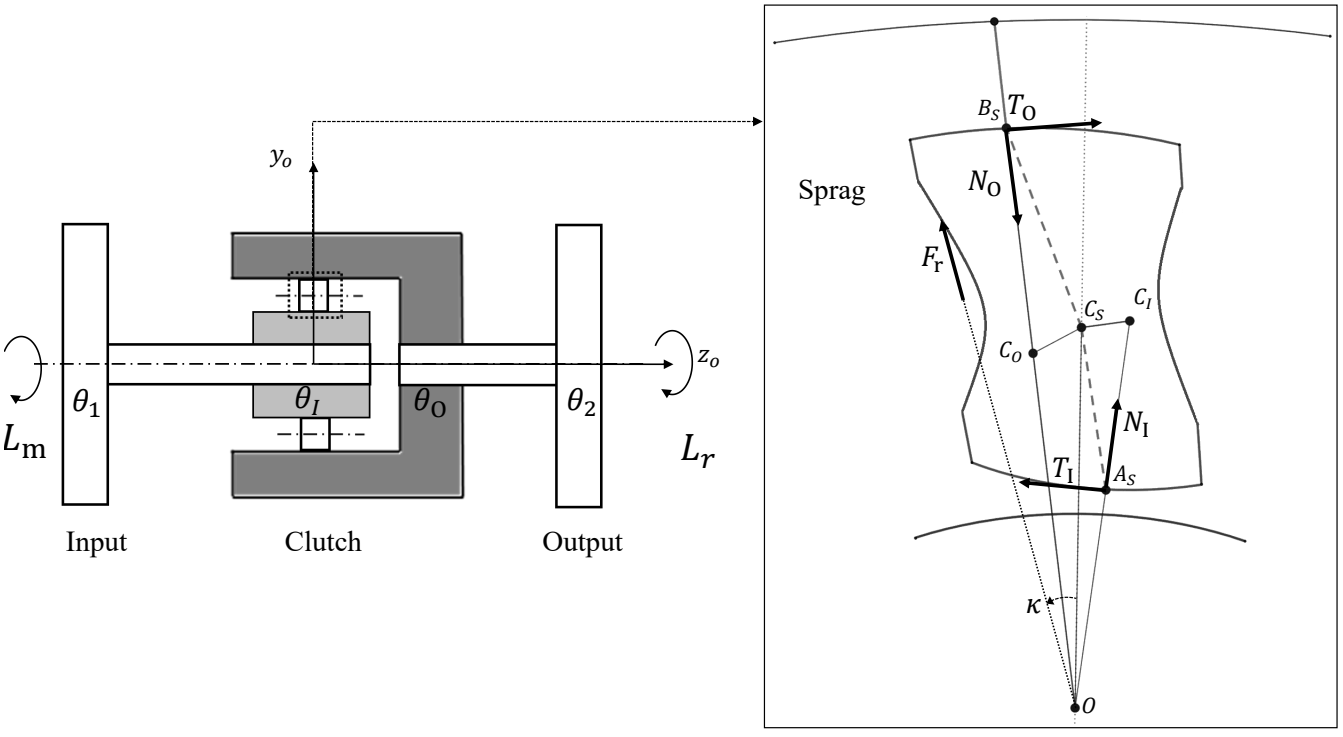


Figure 4. Powertrain model with a sprag overrunning clutch: (a) lumped torsional model and (b) free-body diagram of the sprag.

force varies, so that the angle κ between the direction of F_r and the line OC_S becomes a function of the rotation angle α. Let r_p denote the distance between P and C_S, and let α_p denote the angle between $\overline{\mathrm{P}C_S}$ and $\overline{OC_S}$ in the reference configuration ($\alpha = 0$). The angle κ is then expressed as a function of the sprag angle α:

$$\kappa(\alpha) = \arctan\left(\frac{r_\mathrm{p}\sin(\alpha_\mathrm{p} - \alpha)}{\overline{OC_S} + r_\mathrm{p}\cos(\alpha_\mathrm{p} - \alpha)}\right).$$

The motor is represented by the rotational inertia I_1. The shaft connecting the motor to the inner race is modeled by the torsional stiffness K_1 and damping coefficient D_1. The inertia of the inner race and the components rigidly attached to it is denoted by I_I. Similarly, I_O denotes the inertia of the outer race and its associated components. The output shaft connecting the outer race to the propeller is modeled using the torsional stiffness K_2 and damping coefficient D_2, while the propeller is represented by the rotational inertia I_2.

https://doi.org/10.5194/ms-2026-199
Preprint. Discussion started: 19 November 2026
© Author(s) 2026. CC BY 4.0 License.



mechanical sciences
DISCUSSIONS

By enforcing the rotational and translational equilibrium of the powertrain components and of the sprag, the governing equations of motion are obtained as

$$
\begin{aligned}
&I_1\ddot{\theta}_1 + D_1(\dot{\theta}_1 - \dot{\theta}_I) + K_1(\theta_1 - \theta_I) = L_m(t),\\
&I_I\ddot{\theta}_I + D_1(\dot{\theta}_I - \dot{\theta}_1) + K_1(\theta_I - \theta_1) = N_s R_I T_I,\\
&m_I\ddot{r}_I + K_{r,I} r_I = -N_I,\\
&I_O\ddot{\theta}_O + D_2(\dot{\theta}_O - \dot{\theta}_2) + K_2(\theta_O - \theta_2) = N_s R_O T_O,\\
&m_O\ddot{r}_O + K_{r,O} r_O = -N_O,\\
&I_2\ddot{\theta}_2 + D_2(\dot{\theta}_2 - \dot{\theta}_O) + K_2(\theta_2 - \theta_O) = L_r,\\
&I_s(\ddot{\alpha} + \ddot{\phi}) + D_\alpha\dot{\alpha} = -b_O T_O - b_I T_I + h_I N_I + h_O N_O - F_r\overline{OC_S}\sin\kappa,\\
&-m_s\overline{OC_S}\ddot{\phi} = \cos\beta_O T_O - \cos\beta_I T_I + \sin\beta_I N_I + \sin\beta_O N_O - F_r\sin\kappa.\\
&m_s\ddot{r}_S = N_I\cos\beta_I - N_O\cos\beta_O + F_r\cos\kappa.
\end{aligned}
\tag{7}
$$

The geometric parameters appearing in Eq. 7 are defined in Figs. 2 and 4. The quantities I_s, m_s, and N_s denote the moment of inertia of a single sprag, the sprag mass, and the number of sprags, respectively. The masses and radial stiffnesses of the inner and outer races are denoted by m_I, m_O, $K_{r,I}$, and $K_{r,O}$, respectively. The coefficients D_α is the viscous damping coefficient associated with the generalized coordinates α. The output torque L_r includes the propeller aerodynamic resistance and any additional torque applied to the output shaft. It is written as

$$L_r = -L_{\text{aero}} + L_{\text{turbo}}, \tag{8}$$

where L_{aero} is assumed to be a quadratic function of the output angular velocity, and L_{turbo} represents the torque provided by the turbine.

Introducing the generalized coordinate vector

$$\mathbf{q} = \begin{bmatrix}\theta_1 & \theta_I & r_I & \theta_O & r_O & \theta_2 & \alpha & \phi & r_S\end{bmatrix}^T, \tag{9}$$

Eq. 7 can be written in compact form as

$$\mathbf{M}\ddot{\mathbf{q}}(t) + \mathbf{C}\dot{\mathbf{q}}(t) + \mathbf{K}\mathbf{q}(t) = \mathbf{L}_{\text{ext}}(t) + \mathbf{L}_{\text{NL}}(\mathbf{q}, \dot{\mathbf{q}}). \tag{10}$$

Here, $\mathbf{M}$ is the mass matrix, while $\mathbf{C}$ and $\mathbf{K}$ are the damping and stiffness matrices. The vector $\mathbf{L}_{\text{ext}}$ collects the externally applied torques, and $\mathbf{L}_{\text{NL}}$ contains the nonlinear load contributions, including those associated with the contact forces and the aerodynamic load.

https://doi.org/10.5194/ms-2026-199
Preprint. Discussion started: 19 November 2026
© Author(s) 2026. CC BY 4.0 License.



mechanical sciences
DISCUSSIONS

The nonlinear load vector is written as

$$\mathbf{L}_{\mathrm{NL}} = \begin{bmatrix} 0 \\ N_s R_I T_I \\ -N_I \\ N_s R_O T_O \\ -N_O \\ -C_{\mathrm{aero}} \dot{\theta}_2^2 \\ -b_O T_O - b_I T_I + h_I N_I + h_O N_O - F_r \overline{OC_S} \sin\kappa \\ (\cos\beta_O T_O - \cos\beta_I T_I + \sin\beta_I N_I + \sin\beta_O N_O - F_r \sin\kappa)/\overline{OC_S} \\ N_I \cos\beta_I - N_O \cos\beta_O \ + F_r \cos\kappa \end{bmatrix} \tag{11}$$

The external loads may drive the system into either engaged or overrunning operation, depending on their temporal evolution and relative magnitude.

For numerical integration, the state vector is defined as $\mathbf{y}(t) = \begin{bmatrix} \mathbf{q}^T & \dot{\mathbf{q}}^T \end{bmatrix}^T$. The equations of motion can then be written in state-space form as

$$\dot{\mathbf{y}} = -\mathbf{Z}\mathbf{y} + \mathbf{f}, \tag{12}$$

with

$$\mathbf{Z} = \begin{bmatrix} \mathbf{0} & -\mathbf{I} \\ \mathbf{M}^{-1}\mathbf{K} & \mathbf{M}^{-1}\mathbf{C} \end{bmatrix}, \qquad \mathbf{f} = \begin{bmatrix} \mathbf{0} \\ \mathbf{M}^{-1}\left[\mathbf{L}_{\mathrm{ext}}(t) + \mathbf{L}_{\mathrm{NL}}(\mathbf{q}, \dot{\mathbf{q}})\right] \end{bmatrix}. \tag{13}$$

Equation 12 is integrated in time using an explicit scheme, such as a fourth-order Runge–Kutta method. At each time step, the contact geometry is updated, the local relative displacements are evaluated, and the normal and tangential contact forces are computed using the displacement-based contact model described in Section 2.1.2.

2.2 Optimization formulation

The geometric optimization is performed for prescribed inner- and outer-race radii, R_I and R_O. Five variables define the two circular sprag cams and their positions relative to the sprag centroid C_S:

$$\mathbf{x} = [\xi_i,\ R_{s,i},\ a_i,\ a_o,\ \xi_o]^T. \tag{14}$$

Here, a_i and a_o are the distances from C_S to the inner- and outer-cam curvature centers, ξ_i and ξ_o specify their angular positions (Fig. 5), and $R_{s,i}$ is the inner-cam radius. The outer-cam radius $R_{s,o}$ and the radial location $\overline{OC_S}$ are derived by imposing zero initial clearance at both interfaces. The remaining contact-geometric quantities are computed as described in Appendix A.

For each geometrically feasible candidate, the complete transient simulation is performed under the same prescribed torque and preload histories. During the simulation, the contact law of Section 2.1.2 identifies stick, slip, and lift-off at both interfaces.

https://doi.org/10.5194/ms-2026-199
Preprint. Discussion started: 19 November 2026
© Author(s) 2026. CC BY 4.0 License.



mechanical sciences
DISCUSSIONS

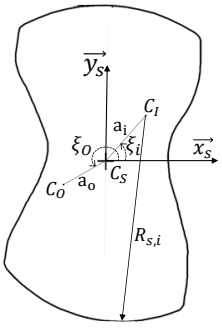


Figure 5. Five design variables defining the inner and outer sprag cams.

Slippage failure is detected when either interface enters the slip state after the preload phase; rollover is detected when the absolute sprag rotation reaches its prescribed limit, $\alpha_{\lim}$. The integration stops at the first detected failure or at the end of the prescribed time interval. Denote the stopping time by $t_s(\mathbf{x})$ and the corresponding applied motor torque magnitude by $L_s(\mathbf{x}) = |L_m(t_s;\mathbf{x})|$.

The solver also returns the maximum contact-stress measure attained up to the stopping time,

$$\sigma_{\max}(\mathbf{x}) = \max_{k\in\{I,O\}} \max_{0\le t\le t_s(\mathbf{x})} \sigma_k(t;\mathbf{x}). \tag{15}$$

The contact stress is evaluated separately using the nominal Hertzian line-contact formulation adopted by Kish (1977). Accordingly, the maximum contact pressure at interface $k \in \{I,O\}$ is estimated as

$$\sigma_k(t) = \sqrt{\frac{N_k(t)E^*}{\pi \ell_{\text{eff}} R_k^*(t)}}, \tag{16}$$

where $N_k(t)$ is the total normal force acting on one sprag–race interface, ℓ_{eff} is the effective axial contact length, and E^* and $R_k^*(t)$ are the equivalent elastic modulus and curvature radius, respectively, defined as

$$\frac{1}{E^*} = \frac{1-\nu_1^2}{E_1} + \frac{1-\nu_2^2}{E_2}, \qquad \frac{1}{R_I^*} = \frac{1}{R_{s,i}} + \frac{1}{R_I}, \qquad \frac{1}{R_O^*} = \frac{1}{R_{s,o}} - \frac{1}{R_O}. \tag{17}$$

The effective contact length is taken equal to the sprag axial length, assuming nominally uniform loading along the contact line. Thus, the computed stress represents a nominal maximum Hertzian pressure, without accounting for possible axial load concentration or edge effects.

The fitness function combines the applied motor torque at failure onset with the maximum nominal contact pressure as

$$J(\mathbf{x}) = \left[\frac{L_{m,\text{target}}}{L_s(\mathbf{x})}\right]^2 \frac{\sigma_{\max}(\mathbf{x})}{\sigma_{\text{ref}}}, \qquad \sigma_{\text{ref}} = 3.1\ \text{GPa}, \tag{18}$$

where $L_{m,\text{target}}$ is the prescribed peak input torque. Minimizing this scalar fitness favours candidates that sustain a larger portion of the imposed loading history while exhibiting lower computed contact stress. This is a stress-weighted failure-onset

https://doi.org/10.5194/ms-2026-199
Preprint. Discussion started: 19 November 2026
© Author(s) 2026. CC BY 4.0 License.



mechanical sciences
DISCUSSIONS

objective, not a direct maximization of a separately computed torque capacity. If no failure occurs before the end of the simulation, L_s represents the applied torque at termination rather than a demonstrated failure threshold.

The implemented optimization problem is

$$\begin{aligned} &\min_{\mathbf{x}} \quad J(\mathbf{x}), \\ &\text{subject to} \quad g_j(\mathbf{x}) \le 0, \quad j = 1, \dots, 4, \\ &\qquad\qquad \mathbf{x}_{\min} \le \mathbf{x} \le \mathbf{x}_{\max}. \end{aligned} \tag{19}$$

The four nonlinear inequalities applied in the current implementation are geometric. With $\Delta R = R_O - R_I$, they are

$$\Delta R - R_{s,i} - R_{s,o} - a_i - a_o \le 0, \tag{20}$$

$$0.1\Delta R - (\overline{OC_S} - R_I) \le 0,$$

$$(\overline{OC_S} - R_I) - 0.9\Delta R \le 0, \tag{21}$$

$$0.05\ \text{mm} - R_{s,o} \le 0. \tag{22}$$

These conditions restrict the cam-center construction, keep the sprag centroid within the central 80% of the radial gap, and require a positive minimum outer-cam radius. Although stress, rotation, and contact state are monitored during each simulation, the present code does not impose separate dynamic nonlinear inequalities in `ga`; their influence enters through simulation termination and the fitness function.

3 Numerical analysis

For the numerical simulations, a set of parameters representative of the powertrain model introduced in Fig. 4 is adopted. After setting these parameters in the following, the transient response of the powertrain is evaluated first for a reference sprag geometry in Sec. 3.1. This analysis is used to demonstrate how the displacement-based contact model predicts the contact states and how the slippage and rollover criteria are checked during acceleration. Then the optimization results are given in Sec. 3.2.

The powertrain and clutch parameters are reported in Tables 1 and 2. The employed system of unit is N–mm–tonne.

Table 1. Powertrain parameters used in the numerical simulations.

Parameter	Value	Parameter	Value
K_1 [N mm/rad]	5×10^6	K_2 [N mm/rad]	5×10^5
I_1 [tonne mm^2]	157	I_2 [tonne mm^2]	400
D_α [N mm s/rad,]	0.823	D_{aero} N mm s^2/rad^2	10
D_1 [N mm s/rad]	3.56	D_2 [N mm s/rad]	25.8

The shaft damping coefficients (D_1 and D_2) and D_α represent equivalent drivetrain dissipation and are selected to obtain a damping ratio of 0.016 for the first elastic mode of the linearized, fully sticking engaged configuration.

https://doi.org/10.5194/ms-2026-199
Preprint. Discussion started: 19 November 2026
© Author(s) 2026. CC BY 4.0 License.



mechanical sciences
DISCUSSIONS

Table 2. Clutch parameters used in the numerical simulations.

Parameter	Value	Parameter	Value
R_I [mm]	19.046	R_O [mm]	27.374
I_s [tonne mm^2]	1.2×10^{-5}	m_s [tonne]	1.8×10^{-6}
I_I [tonne mm^2]	0.03	I_O [tonne mm^2]	0.3
m_I [tonne]	3.0×10^{-4}	m_O [tonne]	8.6×10^{-4}
$K_{r,I}$ [N/mm]	3.8×10^{7}	$K_{r,O}$ [N/mm]	2.2×10^{7}
N_s	18	r_p [mm]	1.18
α_p	67°		

The normal contact force is evaluated using the Hertzian law introduced in Eq. 4. Following Xu and Lowen (Xu and Lowen, 1994), two point contacts are assumed along the axial direction of the sprag. Their comparison of line-contact, single-point-contact, and two-point-contact representations showed that the two-point-contact model provided the closest agreement with the experimental observations. The Hertzian coefficient for one-point contact is computed as

$$K_H = \frac{4}{3} E^* \sqrt{R^*}, \tag{23}$$

where E^* and R^* are the equivalent elastic modulus and radius, respectively.

The tangential contact stiffness is evaluated from the elastic tangential response of a circular point contact under sticking conditions (Johnson, 1987). The tangential force is written as

$$T = 8 G^* a u_t, \tag{24}$$

where u_t is the tangential relative displacement, G^* is the equivalent shear modulus, and a is the contact radius (Eq. **??**). For identical materials,

$$\frac{1}{G^*} = \frac{2(2-\nu)}{G}, \tag{25}$$

and the total tangential stiffness of the two axial point contacts is

$$K_t = 2\,(8 G^* a)\,, \tag{26}$$

The Hertzian coefficients at the inner and outer contacts are computed from the geometric and material properties of the races and sprags. Because the tangential contact stiffness depends on the instantaneous normal load through the contact radius, K_t is updated at every time step.

The same material properties are assumed for the sprag and both races, with $E = 206$ GPa and $\nu = 0.3$. The friction coefficient is set to $\mu = 0.1$, consistent with the range 0.07–0.13 previously reported for sprag overrunning clutches and steel–steel frictional contacts (Xue et al., 2022; Dutt et al., 2024).

https://doi.org/10.5194/ms-2026-199
Preprint. Discussion started: 19 November 2026
© Author(s) 2026. CC BY 4.0 License.



mechanical sciences
DISCUSSIONS

3.1 Baseline transient response

The reference sprag geometry used for the transient response analysis and supplied as an initial individual to the genetic algorithm is reported in Table 3.

Table 3. Initial sprag geometric parameters.

a_i [mm]	a_o [mm]	ξ_i [deg]	ξ_o [deg]	$R_{s,i}$ [mm]
0.319	0.300	25.1	244.7	3.580

This set of parameters is selected from data available in the literature (Li et al., 2021; Huang et al., 2018; Lynwander et al., 1972) and preliminary simulations.

The initial normal load required to keep the sprags in contact with the races is provided by the support spring. In practice, this preload is introduced quasi-statically during clutch assembly. Accordingly, each simulation is divided into two stages.

In the first stage, the support-spring force is increased gradually until the prescribed nominal preload is reached. The transient dynamic analysis is then performed. After preloading, the external torques are applied to the motor and propeller sides of the powertrain, and the contact response is monitored throughout acceleration.

For the illustrative baseline case, the adopted maximum input torque and support-spring histories are $150\ \mathrm{N\,m}$ and $50\ \mathrm{N}$, they are shown in Fig. 6(a), and the corresponding output response is shown in Fig. 6(b).

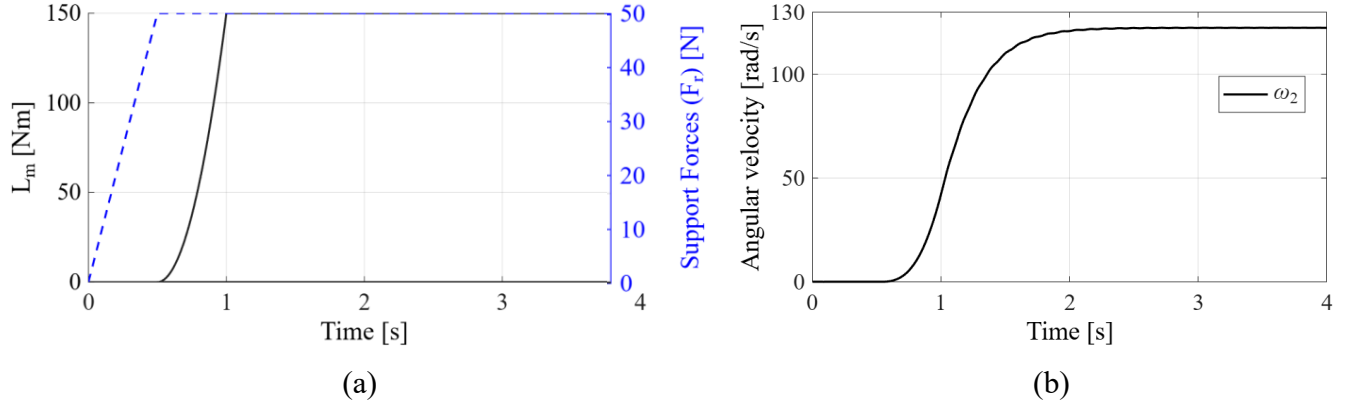


Figure 6. Baseline transient simulation under a maximum input torque of $150\ \mathrm{N\,m}$: (a) input torque and support-spring preload and (b) output angular velocity.

The output response in Fig. 6(b) shows that the clutch remains engaged during the acceleration transient for the selected reference geometry and applied torque. To verify this condition more directly, the Hertzian contact stresses, sprag rotation angle, and inner contact tangential force are reported in Fig. 7.

https://doi.org/10.5194/ms-2026-199
Preprint. Discussion started: 19 November 2026
© Author(s) 2026. CC BY 4.0 License.

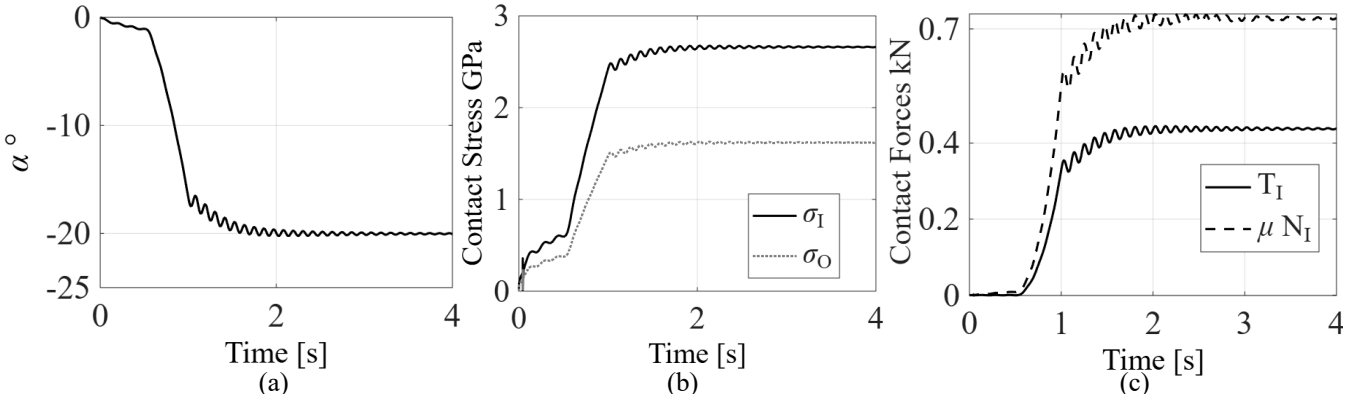


Figure 7. Baseline transient simulation: (a) sprag rotation angle α, (b) inner- and outer-contact stresses, and (c) inner-contact tangential force and Coulomb limit.

Figure 7(a) shows the evolution of the sprag rotation angle α. Rollover is assumed to occur when the magnitude of this angle reaches the admissible limit $\alpha_{\max,\text{allow}} = 30°$. Because $|\alpha|$ remains below this value, rollover does not occur in the baseline simulation.

Figure 7(b) shows the maximum nominal Hertzian contact pressure at the inner and outer contacts. Its mean value after the acceleration transient is $\sigma_{S,I} = 2.66$ GPa, which remains below the material-based allowable value $\sigma_{\text{allow}} = 3.1$ GPa used for this baseline comparison. As a quasi-static verification of the contact-load prediction, the steady engaged-state value is compared with that obtained from the clutch-design formulation of Kish (Kish, 1977); the two estimates are in close agreement. This comparison supports the steady-state stress prediction.

Figure 7(c) shows the inner-contact tangential force and the corresponding Coulomb limit. Because the inner race has the smaller radius, a larger tangential force is required at the inner interface to transmit the same torque. The normal forces at the two interfaces are approximately equal; consequently, the inner contact generally has the larger friction-utilization ratio,

$$\frac{|T_I|}{\mu N_I} > \frac{|T_O|}{\mu N_O}, \tag{27}$$

and is therefore more susceptible to slippage.

An additional simulation is performed to demonstrate the importance of the loading rate. The torque ramp-up time is reduced while all geometric parameters are held fixed. The resulting sprag rotation and inner-contact stress are shown in Fig. 8.

When the ramp-up time is reduced to one-tenth of its baseline value, the maximum sprag rotation and contact stress increase by approximately 25% and 12%, respectively. The clutch therefore approaches both design limits more closely. This result demonstrates that a quasi-static calculation alone cannot determine the required safety margins and that the loading history must be included in the design evaluation.

https://doi.org/10.5194/ms-2026-199
Preprint. Discussion started: 19 November 2026
© Author(s) 2026. CC BY 4.0 License.

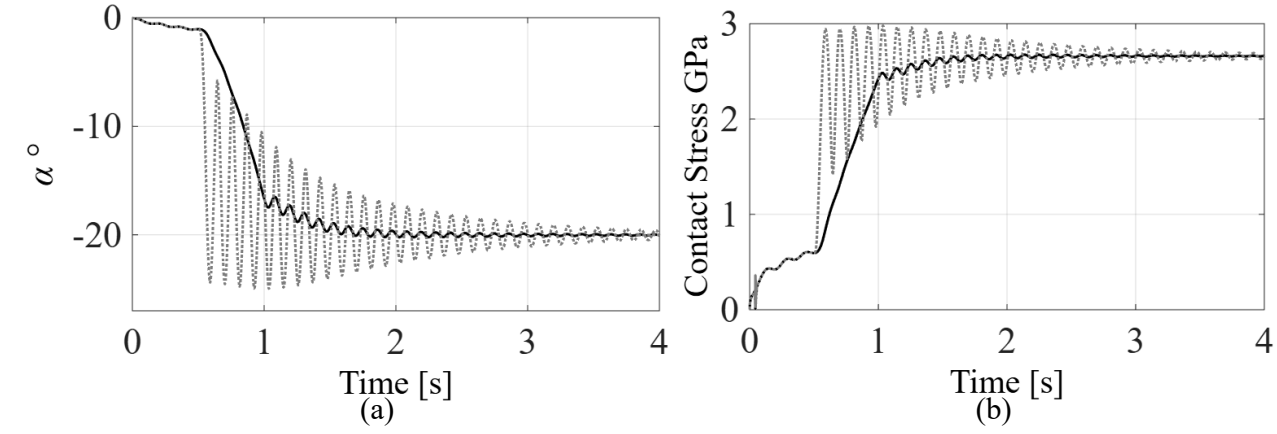


Figure 8. Effect of reducing the torque ramp-up time from 0.5 s (solid line) to 0.05 s (dotted line) on (a) sprag rotation and (b) inner-contact stress.

3.2 Genetic-algorithm implementation and results

The five geometric design variables are optimized using MATLAB's `ga` solver. Each individual represents a candidate sprag geometry, for which the geometric constraints are checked and the nonlinear transient response is evaluated. The simulation is terminated when slippage or rollover is detected, or when the prescribed integration interval is completed. The torque reached at termination and the maximum contact stress are then used to evaluate the objective function defined in Eq. 18. To avoid repeated simulations, the results are cached using the full-precision design vector as a key.

The design-variable bounds are reported in Table 4, while the reference geometry in Table 3 is included in the initial population.

Table 4. Bounds of the geometric design variables.

Variable	Lower bound	Upper bound
ξ_i [deg]	ε	$90-\varepsilon$
$R_{s,i}$ [mm]	$\Delta R/4$	ΔR
a_i [mm]	ε	$1-\varepsilon$
a_o [mm]	ε	$1-\varepsilon$
ξ_o [deg]	$90-\varepsilon$	$270-\varepsilon$

Here, $\varepsilon = 10^{-6}$ and $\Delta R = R_O - R_I$. The race radii are fixed at $R_I = 19.046$ mm and $R_O = 27.374$ mm. The optimization simulations use a peak input torque of 1500 N m, a torque ramp-up time of 0.1 s, and a support-spring preload of 50 N.

https://doi.org/10.5194/ms-2026-199
Preprint. Discussion started: 19 November 2026
© Author(s) 2026. CC BY 4.0 License.



mechanical sciences DISCUSSIONS

Table 5 reports the initial geometry, two intermediate candidates, and the best candidate identified by the genetic algorithm, together with their corresponding slippage-onset torques and maximum contact stresses. Slippage is the limiting failure mechanism for all four designs.

Table 5. Selected geometries and corresponding slippage-onset torque and maximum contact stress. C1 and C2 denote intermediate candidates identified during optimization.

Design	a_i [mm]	a_o [mm]	ξ_i [deg]	ξ_o [deg]	$R_{s,i}$ [mm]	L_s [N m]	$\sigma_{\max}$ [GPa]
Initial	0.319	0.300	25.1	244.7	3.580	544.1	3.23
C1	0.402	0.650	23.3	251.591	4.815	680.0	2.85
C2	0.402	0.650	23.3	107.8	3.815	739.4	3.36
Best	0.344	0.656	23.5	231.7	4.823	777.1	2.83

The results demonstrate the strong influence of sprag geometry on torque capacity. The slippage-onset torque increases from 544.1 N m for the initial design to 777.1 N m for the best candidate, corresponding to an improvement of approximately 42.8%. Meanwhile, the maximum contact stress decreases from 3.23 to 2.83 GPa, remaining below the allowable limit of 3.1 GPa for the best candidate. Thus, the optimized geometry improves torque-transmission capability while its computed stress is below the prescribed allowable value.

To examine the dynamic behavior of the selected geometries under identical loading conditions, the four designs are subjected to the transient load history defined in Section 3.1. The resulting maximum contact stress, sprag rotation, and minimum frictional capacity-to-demand ratio at the inner contact are reported in Table 6.

Table 6. Transient response of the representative geometries under the same prescribed loading condition.

Design	$\sigma_{\max}$ [GPa]	α_{peak} [deg]	$\min_t \left(\frac{\mu N_I}{\lvert T_I \rvert}\right)$
Initial	3.01	-25.5	1.73
C1	2.61	-15.9	1.30
C2	2.31	-14.9	1.27
Best candidate	2.12	-10.13	1.03

Under the same applied torque, the best candidate exhibits a lower maximum contact stress and a smaller sprag rotation. Compared with the initial design, the maximum stress decreases by approximately 30%, while the magnitude of the peak sprag rotation decreases by approximately 60%. These results indicate that the optimized geometry reduces both contact-stress demand and the tendency toward rollover under the considered loading condition.

However, these improvements are accompanied by a reduction in the frictional safety margin. The ratio $\mu N_I/|T_I|$ compares the available friction capacity with the tangential force required for torque transmission. A value greater than unity indicates that the contact remains within the Coulomb friction limit, whereas a value approaching unity indicates an increasing tendency

https://doi.org/10.5194/ms-2026-199
Preprint. Discussion started: 19 November 2026
© Author(s) 2026. CC BY 4.0 License.



mechanical sciences
DISCUSSIONS

toward slippage. As shown in Table 6, the minimum ratio decreases from 1.73 for the initial design to 1.03 for the best candidate.

The results reveal an important trade-off between contact stress, sprag rotation, and frictional safety margin. Although the best candidate achieves a higher slippage-onset torque and lower stress and rotation under the prescribed comparison load, it operates closer to the friction limit. Since the friction coefficient may vary during clutch operation, optimization based on its nominal value may lead to designs with limited robustness to friction uncertainty. A more conservative approach is to perform the optimization using a lower friction coefficient or impose a minimum frictional safety margin as an additional constraint.

To investigate this aspect, the optimization is repeated with a reduced friction coefficient of $\mu = 0.08$, instead of the nominal value of $\mu = 0.1$. The resulting geometry and corresponding slippage-onset torque are reported in Table 7. The maximum slippage-onset torque decreases to 672.8 N m, demonstrating the influence of the assumed friction coefficient on the achievable torque-transmission capability and the resulting geometric design.

Table 7. Best geometry identified for $\mu = 0.08$ and its corresponding slippage-onset torque and maximum contact stress.

Design	a_i [mm]	a_o [mm]	ξ_i [deg]	ξ_o [deg]	$R_{s,i}$ [mm]	L_s [N m]	$\sigma_{\max}$ [GPa]
Best candidate	0.402	0.650	24.3	250.5	4.815	672.8	2.85

To compare the resulting design with those optimized using the nominal friction coefficient, the geometry obtained for $\mu = 0.08$ is subsequently evaluated under the same prescribed loading condition, with μ restored to 0.1. The corresponding response measures are reported in Table 8.

Table 8. Transient response of the geometry optimized for $\mu = 0.08$, evaluated under the prescribed comparison load with $\mu = 0.1$.

$\sigma_{\max}$ [GPa]	α_{peak} [deg]	$\min_t \left(\frac{\mu N_I}{\lvert T_I \rvert} \right)$
2.30	-14.6	1.28

Compared with the geometry optimized for $\mu = 0.1$, the design obtained using the lower friction coefficient exhibits a higher frictional capacity-to-demand ratio (1.28 instead of 1.03), indicating a larger margin against slippage under the nominal operating condition. However, its maximum contact stress and sprag rotation are slightly higher. These results illustrate the trade-off between torque-transmission performance and frictional robustness and indicate that the assumed friction coefficient plays an important role in determining the preferred sprag geometry.

4 Conclusions

A failure-aware geometric-optimization framework has been developed to improve the torque-transmission capability of sprag overrunning clutches by integrating transient dynamics analysis with a genetic algorithm. The framework evaluates the competing effects of geometric parameters on contact stress, slippage, and rollover. By computing the failure-onset torque from the

https://doi.org/10.5194/ms-2026-199
Preprint. Discussion started: 19 November 2026
© Author(s) 2026. CC BY 4.0 License.



mechanical sciences
DISCUSSIONS

transient dynamic response and incorporating it into a stress-weighted objective function, the framework identifies favorable combinations of five sprag geometric parameters despite their nonlinear and competing effects on clutch performance.

The numerical results demonstrate the importance of transient loading, as faster torque application increases both contact stress and sprag rotation. The optimization increases the applied motor torque at slippage onset from 544.1 to 777.1 N m (42.8%), while reducing the corresponding maximum contact stress from 3.23 to 2.83 GPa, below the prescribed allowable limit of 3.1 GPa. Under identical loading conditions, the best design reduces the maximum contact stress by 30% and the magnitude of sprag rotation by 60%.

These improvements, however, are accompanied by a reduction in the minimum frictional capacity-to-demand ratio from 1.73 to 1.03, quantifying a trade-off between torque-transmission capability and frictional safety margin. Repeating the optimization with a lower friction coefficient ($\mu = 0.08$) yields a geometry with a higher frictional safety margin (1.28) under nominal conditions ($\mu = 0.1$), although at the expense of increased contact stress and sprag rotation. These findings highlight the importance of considering friction uncertainty in geometric optimization. Future work will consider friction uncertainty more systematically, together with manufacturing tolerances, experimental validation, and more extensive optimization searches.

Appendix A: Computation of clutch geometric parameters

The relative contact displacements cannot be expressed directly as explicit functions of the geometric design parameters. Therefore, a set of auxiliary geometric quantities is introduced to compute the displacement contributions of the sprag contact points induced by rotation about point C_S, and to subsequently project these contributions onto the local contact coordinate systems.

These parameters are first defined for an initial configuration in which the sprag rotation angle α is assumed to be zero. During the transient simulation, they must be updated at each time step to account for the evolving contact location.

In this work, it is assumed that, in the initial configuration, no clearance exists between the sprags and the races. Under this assumption, the distances of the centers of curvature of the sprag arcs from the inertial origin are given by

$$\overline{OC_O} = R_O - R_{s,o}, \qquad \overline{OC_I} = R_I + R_{s,i}, \tag{A1}$$

$$\beta_i = \arccos\left(\frac{\overline{OC_S}^2 + \overline{OC_I}^2 - a_i^2}{2\,\overline{OC_S}\,\overline{OC_I}}\right), \qquad \beta_o = \arccos\left(\frac{\overline{OC_S}^2 + \overline{OC_O}^2 - a_o^2}{2\,\overline{OC_S}\,\overline{OC_O}}\right), \tag{A2}$$

where R_I and R_O denote the radii of the inner and outer races, $R_{s,i}$ and $R_{s,o}$ are the radii of curvature of the inner and outer sprag arcs, and a_i and a_o are the corresponding distances defined by the clutch geometry.

Accordingly, the initial positions of the centers of curvature of the sprag arcs, expressed in the reference frame (x_b, y_b) rotating with point C_S (shown in Fig. 1), are

$$\overrightarrow{OC_{O0}} = \begin{bmatrix} -\sin\beta_o \\ \cos\beta_o \end{bmatrix} \overline{OC_O}, \qquad \overrightarrow{OC_{I0}} = \begin{bmatrix} \sin\beta_i \\ \cos\beta_i \end{bmatrix} \overline{OC_I}. \tag{A3}$$

https://doi.org/10.5194/ms-2026-199
Preprint. Discussion started: 19 November 2026
© Author(s) 2026. CC BY 4.0 License.



mechanical sciences
DISCUSSIONS

The position of the sprag contact points can then be obtained as

$$\overrightarrow{OA_S} = \overrightarrow{OC_I}\left(1 - \frac{R_{s,i}}{\overline{OC_I}}\right). \tag{A4}$$

$$\overrightarrow{OB_S} = \overrightarrow{OC_O}\left(1 + \frac{R_{s,o}}{\overline{OC_O}}\right). \tag{A5}$$

Based on these quantities, the remaining geometric parameters are computed as

$$h_i = \overline{OC_S}\sin\beta_i, \qquad b_i = \overline{OC_S}\cos\beta_i - \overline{OA_S}, \qquad \chi_i = \arctan\left(\frac{h_i}{b_i}\right), \tag{A6}$$

$$h_o = \overline{OC_S}\sin\beta_o, \qquad b_o = \overline{OB_S} - \overline{OC_S}\cos\beta_o, \qquad \chi_o = \arctan\left(\frac{h_o}{b_o}\right). \tag{A7}$$

As the sprag rotates about its centroid C_S through an angle α, all geometric quantities are updated at each time step. The update also accounts for the incremental radial displacement of the sprag:

$$\overline{OC_S}^{n+1} = \overline{OC_S}^{n} + \delta r_S. \tag{A8}$$

The remaining geometric quantities are updated incrementally to account for the rotation and radial displacement of the sprag. The incremental rotation matrix is

$$\mathbf{T}(\delta\alpha) = \begin{bmatrix} \cos(\delta\alpha) & -\sin(\delta\alpha) \\ \sin(\delta\alpha) & \cos(\delta\alpha) \end{bmatrix}. \tag{A9}$$

Accordingly, the positions of the outer and inner cam centers at time step $n+1$ are obtained as

$$\overrightarrow{OC_O}^{n+1} = \overrightarrow{OC_S}^{n+1} + \mathbf{T}(\delta\alpha)\left(\overrightarrow{OC_O}^{n} - \overrightarrow{OC_S}^{n}\right), \tag{A10}$$

$$\overrightarrow{OC_I}^{n+1} = \overrightarrow{OC_S}^{n+1} + \mathbf{T}(\delta\alpha)\left(\overrightarrow{OC_I}^{n} - \overrightarrow{OC_S}^{n}\right). \tag{A11}$$

All remaining geometric parameters are subsequently updated using the same formulations as above, based on the current positions of the centers of curvature of the sprag arcs.

Author contributions. Conceptualization, F.M., S.Z. and C.M.F.; methodology, F.M., S.Z. and C.M.F.; software, F.M.; validation, F.M., S.Z. and C.M.F.; investigation, F.M.; writing—original draft preparation, F.M.; writing—review and editing, F.M., S.Z. and C.M.F.; supervision, S.Z. and C.M.F.; project administration, C.M.F.; funding acquisition, C.M.F. All authors have read and agreed to the published version of the manuscript.

Competing interests. The authors declare no conflicts of interest.

Acknowledgements. This project is supported by the Clean Aviation Joint Undertaking and its members under Grant Agreement No. 101102020 (AMBER). Funded by the European Union. The views and opinions expressed are, however, those of the authors only and do not necessarily

https://doi.org/10.5194/ms-2026-199
Preprint. Discussion started: 19 November 2026
© Author(s) 2026. CC BY 4.0 License.



mechanical sciences
DISCUSSIONS

reflect those of the European Union or the Clean Aviation Joint Undertaking. Neither the European Union nor the granting authority can be held responsible for them.

https://doi.org/10.5194/ms-2026-199
Preprint. Discussion started: 19 November 2026
© Author(s) 2026. CC BY 4.0 License.



mechanical sciences
DISCUSSIONS

References

Overrunning Clutches Application Manual, Formsprag Clutch, https://www.ipcd-inc.com/wp-content/uploads/2019/03/Formsprag-Clutches-and-Backstops.pdf, 2018.

Bouchard, E. D., Verberne, J., D'Arpino, M., Ozcan, M., Porpora, F., Gladin, J., Patel, S., Justin, C., and Mavris, D.: Modeling and simulation of novel electric/hybrid electric multicopter architectures for urban air mobility, in: 2021 AIAA/IEEE Electric Aircraft Technologies Symposium (EATS), pp. 1–24, IEEE, https://doi.org/10.23919/EATS52162.2021.9704826, 2021.

Chen, L. and Chen, Y.: Wedge-shaped track design and contact analysis of overrunning clutches, Proceedings of the Institution of Mechanical Engineers, Part D: Journal of Automobile Engineering, 222, 1647–1656, https://doi.org/10.1243/09544070JAUTO631, 2008.

Dutt, K. A., Joshi, S. J., Shah, D. B., and Prajapati, D.: Experimental investigations and finite element simulation for predicting wear life of overrunning clutches, Engineering Research Express, 6, 035 522, https://doi.org/10.1088/2631-8695/ad62b7, 2024.

Huang, C., Zhao, Y., and Liu, M.: Analytical modeling and optimization of logarithmic sprag clutch considering profile modification, Shock and Vibration, 2018, 4190 303, https://doi.org/10.1155/2018/4190303, 2018.

Johnson, K. L.: Contact mechanics, Cambridge university press, 1987.

Ke, Z., Wei, W., Liu, C., Guo, M., and Yan, Q.: The dynamic wedging and friction characteristics of one-way clutch under transient loads from stator, Tribology International, 152, 106 568, https://doi.org/10.1016/j.triboint.2020.106568, 2020.

Kish, J.: Helicopter freewheel unit design guide, Tech. Rep. USAAMRDL-TR-77-18, Sikorsky Aircraft, 1977.

Li, J., Yan, H., Lin, M., Cai, M., and Hu, X.: Wear of sprag clutch wedge in overrun state under high temperature condition, Advances in Mechanical Engineering, 13, 16878140219965 13, https://doi.org/10.1177/1687814021996513, 2021.

Lynwander, P., Meyer, A., and Chachakis, S.: Sprag overriding aircraft clutch, Tech. Rep. USAAMRDL TR 72-49, 1972.

Mashayekhi, F., Zucca, S., and Firrone, C. M.: Nonlinear Transient Rolling-Contact Dynamics of Sprag Overrunning Clutches, Machines, https://doi.org/10.1243/09544070JAUTO631, 2026.

Menq, C. and Yang, B.: Non-linear spring resistance and friction damping of frictional constraint having two-dimensional motion, Journal of Sound and Vibration, 217, 127–143, https://doi.org/10.1006/jsvi.1998.1739, 1998.

Nagler, N. and Lohrengel, A.: Improved design criterion for frictionally engaged contacts in overrunning clutches, Forschung im Ingenieurwesen, 85, 1053–1063, https://doi.org/10.1007/s10010-021-00496-5, 2021.

Nanda, A.: The propulsive design aspects on the world's first direct drive hybrid airplane, Ph.D. thesis, Embry-Riddle Aeronautical University, 2011.

Pescetto, P., Cocuzza, F., Mashayekhi, F., Ferrari, S., Zucca, S., Firrone, C., and Pellegrino, G.: Electromagnetic and Mechanical Modeling of Medium Voltage PMSM for Hybrid Regional Aircraft in Faulty Conditions, in: 2025 IEEE Energy Conversion Conference Congress and Exposition (ECCE), pp. 1–7, https://doi.org/10.1109/ECCE58356.2025.11260144, 2025.

Petrov, E. and Ewins, D.: Analytical formulation of friction interface elements for analysis of nonlinear multi-harmonic vibrations of bladed disks, J. Turbomach., 125, 364–371, https://doi.org/10.1115/1.1539868, 2003.

Vernay, P. and Ferraris, G.: Comportement dynamique en torsion et en régime transitoire d'un démarreur de moteur d'avion, Mécanique & industries, 7, 147–153, https://doi.org/10.1051/meca:2006029, 2006.

Xu, T. and Lowen, G.: A mathematical model of an over-running sprag clutch, Mechanism and machine theory, 29, 11–23, https://doi.org/10.1016/0094-114X(94)90016-7, 1994.

https://doi.org/10.5194/ms-2026-199
Preprint. Discussion started: 19 November 2026
© Author(s) 2026. CC BY 4.0 License.



mechanical sciences
DISCUSSIONS

Xue, Y., Wang, Z., Chen, D., Tao, S., and Lu, Y.: Design and test of a new type of overrunning clutch, Machines, 10, 1188, https://doi.org/10.3390/machines10121188, 2022.